Highly photon-loss-tolerant quantum computing using hybrid qubits

S. Omkar,[1,*] Y. S. Teo,[1] Seung-Woo Lee,[2] and H. Jeong[1,†]

[1]*Department of Physics and Astronomy, Seoul National University, 08826 Seoul, Korea*

[2]*Center for Quantum Information, Korea Institute of Science and Technology, Seoul, 02792, Korea*

(Received 9 November 2020; accepted 17 February 2021; published 9 March 2021)

We investigate a scheme for topological quantum computing using optical hybrid qubits and make an extensive comparison with previous all-optical schemes. We show that the photon loss threshold reported by Omkar *et al.* [Phys. Rev. Lett. **125**, 060501 (2020)] can be improved further by employing postselection and multi-Bell-state-measurement-based entangling operations to create a special cluster state, known as Raussendorf lattice for topological quantum computation. In particular, the photon loss threshold is enhanced up to 5.7×10^{-3}, which is the highest reported value given a reasonable error model. This improvement is obtained at the price of consuming more resources by an order of magnitude compared with the scheme in the aforementioned reference. Nevertheless, this scheme remains resource-efficient compared with other known optical schemes for fault-tolerant quantum computation.

DOI: 10.1103/PhysRevA.103.032602

I. INTRODUCTION

The quantum optical platforms have not only the advantage of supplying quicker gate operations compared with the decoherence time [1] but also relatively efficient readouts, which makes them suitable platforms and one of the strongest contenders for realizing scalable quantum computation (QC). However, with these platforms, photon loss is ubiquitous which leads to optical qubit loss and is also a major source of noise, i.e., dephasing or depolarizing [1], also known as the computational errors. Noise stands as the major obstacle in the path towards scalable QC. To overcome the effects of noise, we need fault-tolerant schemes that employ quantum error correction (QEC) [2,3]. QEC promises the possibility to realize a scalable QC with faulty qubits, gates, and readouts (measurements), provided the noise level is below a certain *threshold*. This threshold value is determined according to the details of the fault-tolerant (FT) architecture and the associated noise model. Moreover, QEC has also been employed in quantum metrology [4,5] and communication [6–8]. References [9–11] show that QEC codes can also be used for efficiently characterizing quantum dynamical maps that could be either completely positive or not [12,13].

Fault-tolerant schemes implemented with various kinds of optical qubits provide different ranges of tolerance against both qubit loss and computational errors. The parameters that determine the performance of a fault-tolerant optical scheme are (i) photon loss and computational error thresholds and (ii) their operational values, (iii) *logical* error rate and (iv) resources incurred per logical gate operation. Logical error rate is the rate of failure of QEC that results in a residual error at the highest logical level of encoding [2,3]. From the *threshold theorem* [2,14], we know that, when the fault-tolerant optical hardware operates below the noise threshold, the logical error rate can be made arbitrarily close to zero by allocating more resources. Thus, operational values of the noise, i.e., photon loss and computational error rates too, are important parameters because they determine the required resource to attain the target logical error rate.

It has recently been demonstrated that, by using optical hybrid qubits entangled in the continuous-discrete optical domain, many shortcomings faced individually by continuous variable (CV) and discrete variable (DV) qubits can be overcome in linear optical quantum computing [15,16]. In fact, the fault-tolerant quantum computation (FTQC) schemes based on either DV or CV qubits not only tend to have low thresholds and operational values for photon loss and computational error, but they also require extravagant resources to provide arbitrarily small logical error rates. In order to overcome these limitations, the scheme in Ref. [15] uses optical hybrid qubits that combine single-photon qubits [17] together with the coherent-state qubits [18–22] that are a particular type of CV qubits with coherent states. While this scheme offers an improvement in resource efficiency, both the threshold and operational values of the noise remain low as it employs CSS (Calderbank-Shor-Steane) QEC codes [23–25]. Our recent proposal for topological FTQC [16] employing special cluster states of optical hybrid qubits, also known as a *Raussendorf* lattice ($|\mathcal{C}_{\mathcal{L}}\rangle$), exhibits an improvement in both operational and threshold values of photon loss and computational error by an order of magnitude. This hybrid-qubit-based topological FTQC (HTQC) scheme also offers the best resource efficiency.

HTQC uses linear optics, optical hybrid states, and Bell-state measurement (BSM) as entangling operations (EOs) to create a $|\mathcal{C}_{\mathcal{L}}\rangle$. Interestingly, HTQC does not involve postselection, and active switching is hence unnecessary. Furthermore, there is no need for in-line feed-forward operations.

*omkar.shrm@gmail.com

†h.jeong37@gmail.com

Therefore, HTQC is ballistic in nature. In this work we show that, by employing postselection over the successful EOs and using multi-BSM EOs (see Fig. 4) at a certain stage of creation of $|\mathcal{C}_\mathcal{L}\rangle$, the photon-loss threshold, η_{th} can be further improved. We shall also show that this improvement costs more resources than the HTQC, but only by an order of magnitude.

The rest of the article is organized as follows: In Sec. II, we briefly explain the preliminaries of measurement-based fault-tolerant topological QC on a $|\mathcal{C}_\mathcal{L}\rangle$. Readers familiar with the topic can skip this section. In Sec. III we describe our scheme that employs postselection and multi-BSM-based EOs to build $|\mathcal{C}_\mathcal{L}\rangle$ using hybrid qubits. Furthermore, in Sec. IV, we detail the generation of star cluster states used as building-blocks for $|\mathcal{C}_\mathcal{L}\rangle$. In Sec. V, we describe the noise model used and simulation procedure of QEC is outlined in Sec. VI. In Sec. VII, we present our results on the improved photon loss thresholds, and the details about resource estimation is provided in the Sec. VIII. In Sec. IX, we compare the various performance parameters of our scheme with those of other schemes for optical FTQC. Finally, the discussion and conclusion are presented in Sec. X.

II. PRELIMINARIES

In this section we briefly review the measurement-based fault-tolerant topological QC on $|\mathcal{C}_\mathcal{L}\rangle$. For this purpose, we first define what the cluster states are in general and describe measurement-based FTQC on them. As an alternative to the circuit-based model for QC, Raussendorf and Briegel [26] developed a model where a universal set of gates can be realized using only adaptive single-qubit measurements in different bases on a multiqubit entangled state known as cluster state. In general, a cluster state $|\mathcal{C}\rangle$ over a collection of qubits $\mathcal{C}$ is a state stabilized by the operators $X_a \bigotimes_{b\in \text{nh}(a)} Z_b$, where $a, b \in \mathcal{C}$, Z_i and X_i are the Pauli operators on the ith qubit, and nh(a) denotes the adjacent neighborhood of qubit $a \in \mathcal{C}$. A multiqubit $|\mathcal{C}\rangle$ has the form

$$|\mathcal{C}\rangle = \prod_{b\in \text{nh(a)}} \text{CZ}_{a,b}|+\rangle_a|+\rangle_b \;\forall\; a \in \mathcal{C}, \tag{1}$$

where $|\pm\rangle = (|0\rangle \pm |1\rangle)/\sqrt{2}$ is the eigenstate of X, while $|0\rangle, |1\rangle$ are those of Z. $\text{CZ}_{a,b}$, an EO, applies Z on the target qubit b if the source qubit a is in the state $|1\rangle$. The *unit cell* shown in Fig. 1(a) is an example of a cluster state. This measurement-based QC model is not fault tolerant by nature and, in order to achieve robustness against noise, the cluster qubits were encoded into five-qubit QEC codes [27] and Steane QEC codes [28].

Another route to fault tolerance is to recognize that certain cluster states correspond to topological QEC codes. *Surface codes*, a class of topological QEC codes on two-dimensional (2D) cluster states are known to provide a high error threshold of ≈1% [29] against computational errors. It is known that surfaces codes can tolerate neither qubit-loss nor EO failures, and thus are not suitable for optical platforms [30,31]. The shortcomings of surface codes can be overcome by using a $|\mathcal{C}_\mathcal{L}\rangle$ for topological QEC. For a review on the topic refer to Refs. [32–34]. Topological QEC on $|\mathcal{C}_\mathcal{L}\rangle$ [35] is known to provide a high error threshold of 0.75% [36,37] against computational errors that occur during preparation, storage, gate application, and measurement. In addition, $|\mathcal{C}_\mathcal{L}\rangle$ can tolerate qubit loss [33,38] and *missing edges* [39] due to failed EOs, making it suitable for linear optical platforms.

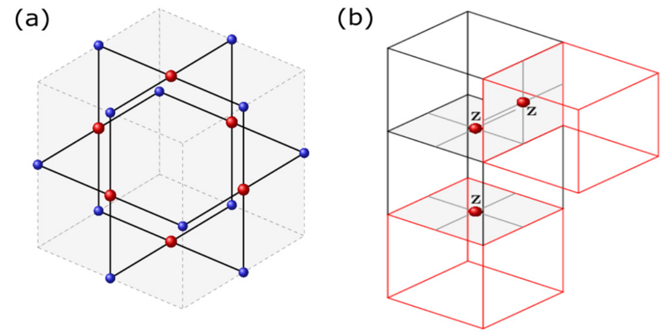

FIG. 1. (a) A unit cell that makes up the lattice $|\mathcal{C}_\mathcal{L}\rangle$. The qubits in red (larger) on the faces of the unit cell correspond to the primal lattice and the others in blue (smaller) correspond to the dual lattice. The black (thick) lines represent the presence of entanglement between the qubits. (b) A string of phase-flip errors will have detection events (red cells) only at the endpoints.

A. Error detection and correction

The lattice $|\mathcal{C}_\mathcal{L}\rangle$ can be thought of as a lattice formed by unit-cell arrangement as shown in the Fig. 1(a). This lattice has qubits mounted on its faces and edges [35]. For QEC and QC, it is important to recognize that $|\mathcal{C}_\mathcal{L}\rangle$ is formed by two interlocking types of lattices, namely, the primal and dual lattices. The dual lattice is a result of mapping the face qubits of the primal lattice to edge qubits and vice versa. From Eq. (1), it is clear that each face of a unit cell is stabilized by $X_i \bigotimes_b Z_b$ where X_i denotes the X operator on the ith face of the unit cell and Z_b denotes the Z operators on the boundary of the face. A stabilizer of a unit cell associated with the primal lattice is given by the product of six constituent face stabilizers, i.e., $S_p = X_1X_2X_3X_4X_5X_6$. To measure S_p, one needs to perform single-qubit measurements in the X basis and multiply the individual outcomes. When there is no phase-flip error on an odd number of qubits, the measurement outcome would be $s_p = +1$.

As the Z operator on an odd number of face qubits anticommute with the S_p, the stabilizer measurement outcome would be $s_p = -1$. On the other hand, an even number of phase-flips go undetected because they commute with S_p and have $s_p = +1$. Therefore, when $s_p = -1$, one can only detect but not locate the errors. An error can be detected and located on $|\mathcal{C}_\mathcal{L}\rangle$ by measuring S_p of the adjacent cubes as shown in Fig. 1(b). Multiple errors on the adjacent cells form an error chain in $|\mathcal{C}_\mathcal{L}\rangle$ that can be detected at its endpoints with the value $s_p = -1$, as shown in Fig. 1(b). However, this only reveals the existence of an error chain, but does not locate every error. Thus, one would need to guess the most likely error chain and apply appropriate corrections. This guess can be carried out by using the efficient minimum weight perfect matching algorithm (MWPM) [40]. MWPM can make wrong guesses and may lead to *logical errors* discussed in the subsequent section. We note that the bit-flip errors on $|\mathcal{C}_\mathcal{L}\rangle$ have

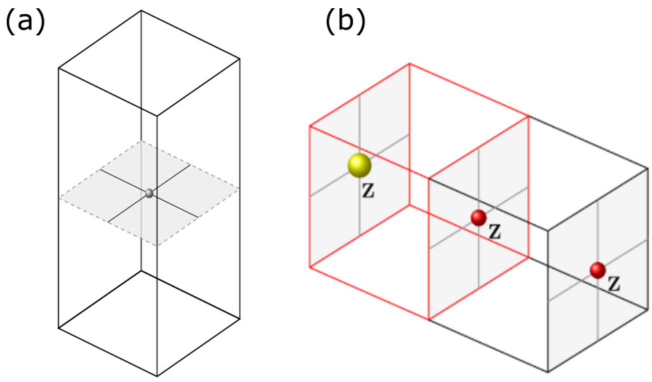

FIG. 2. (a) The qubit on the common face of adjacent cells is considered to be lost. Stabilizers of the two adjacent cells can be multiplied to form a larger cell, which removes the dependency on the measurement outcome of the shared qubit. This feature is employed to deal with qubit loss of unit cells where the larger cell can perform error detection that is not possible by incomplete unit cells. (b) Two unit cells forming a distance $d = 3$ code is shown. Both errors (bigger yellow ball) on a single qubit and two qubits (smaller red balls) cause the same detection events indicated by red cell. Because the single-error case has smaller weight, the MWPM always chooses it even if the errors occurred on two qubits. When the error inference is wrong, making error corrections by applying Z on the larger qubit will complete the error chain connecting the two boundaries, causing a logical error.

trivial effect and thus only the phase flips are of concern in this QEC scheme.

To detect errors on qubits other than those on the faces, we invoke the concept of the dual lattice where the edge qubits in the primal lattice are now the face qubits. One can construct a unit cell and stabilizer S_d on the dual lattice and carry out QEC just like the procedures on the primal lattice. It is important to note that QEC on both type of lattices proceeds independently.

Handling qubit losses. When the qubits in the lattice are lost, it becomes impossible to measure the stabilizers S_p or S_d and detect the errors. To circumvent this issue, one can form a larger stabilizer by multiplying the two adjacent-cell stabilizers such that the lost qubit is shared between them. This eliminates the dependency of the stabilizer on the lost qubit, as shown in Fig. 2(a). The resultant stabilizer with $10X$ operators can perform error detection just like a regular stabilizer of a unit cell. If there are a chain of losses, the same procedure can be extended to form larger cells that can replace unit cells [38].

B. Logical operations and logical errors

A few chosen qubits are measured in the Z basis to create defects that initialize the logical states on the $|\mathcal{C}_{\mathcal{L}}\rangle$. This removes the qubits from the lattice and disentangles the qubits inside the measured region from the rest of the lattice. Depending on the chosen lattice type, the logical qubits would either be of primal or dual types. Logical operations on the logical states correspond to a chain of Z operators that either encircles a defect or connects two defects of the same type [35,36]. Equivalently, in the absence of defects, a logical error happens when boundaries of the same the type are connected by a chain of Z operators.

The code distance d is defined as the minimum number of Z operations required to change the logical state of $|\mathcal{C}_{\mathcal{L}}\rangle$. Errors on the logical states can also be introduced due to the wrong inference by the MWPM during QEC. An error chain of length $(d+1)/2$ or longer can lead to such wrong inferences. For example, consider two cells as shown in the Fig. 2(b), forming a distance $d = 3$ code where both the single-qubit error (bigger ball) and the two-qubit error (smaller balls) cause the same detection events. As the single-error case has smaller weight, the MWPM preferentially chooses it even when errors have actually occurred on the other two qubits. In this case, performing error correction by applying a single Z (on the larger qubit) will connect the two boundaries, causing a logical error.

C. Universal gates

Once a faulty $|\mathcal{C}_{\mathcal{L}}\rangle$ with missing qubits and phase-flip errors is available, topological FTQC is carried out by making sequential single-qubit measurements in the X and Z bases as dictated by the quantum algorithm being implemented. These defects are braided to achieve two-qubit logical operations topologically [35,36]. The lattice qubits are measured in the X basis, the outcomes of which not only provide error syndromes but also effect Clifford gates on the logical states. It is to be noted that not only tolerance against qubit losses but also two-qubit logical operations become available by moving from surface codes to 3D cluster-based QEC codes. The universal set of operations for QC is complete with inclusion of *magic-state distillation* for which measurements on the chosen qubits are carried out in the $(X \pm Y)/\sqrt{2}$ basis [35,36].

III. RAUSSENDORF LATTICE WITH POSTSELECTION AND MULTI-BELL-STATE-MEASUREMENT ENTANGLING OPERATION

In this work, similarly to HTQC, a $|\mathcal{C}_{\mathcal{L}}\rangle$ is created with optical hybrid qubits of the form

$$|\Psi_\alpha\rangle = (|\alpha\rangle|\mathrm{H}\rangle + |-\alpha\rangle|\mathrm{V}\rangle)/\sqrt{2}, \qquad (2)$$

where $|\mathrm{H}\rangle$, $|\mathrm{V}\rangle$ are the discrete orthonormal polarization eigenkets of Z, and $\{|\alpha\rangle|\mathrm{H}\rangle, |-\alpha\rangle|\mathrm{V}\rangle\}$ forms the computational basis for hybrid qubits where α is assumed to be real without loss of generality. However, here we add two extra features; *postselection* and the *multi-BSM EO* to improve η_{th} over HTQC. Employing postselection (choosing the states conditioned on specific measurement outcomes) on the successful BSMs at a certain stage of the current scheme will avoid the formation of undesired *diagonal* edges [refer to Fig. 2(c) of Ref. [16]] and thus resulting in a better $|\mathcal{C}_{\mathcal{L}}\rangle$. Employing the multi-BSM EOs will reduce the value of α required to build $|\mathcal{C}_{\mathcal{L}}\rangle$. We demonstrate in Sec. V that the use of larger α invites larger dephasing on the hybrid qubits in the presence of photon loss. Therefore, using hybrid qubits of smaller values of α would improve the performance against photon loss as dephasing is mitigated. We show that adding these two features in building $|\mathcal{C}_{\mathcal{L}}\rangle$ will lead to an improved η_{th} over HTQC. Henceforth, we shall refer to BSM on hybrid qubits as

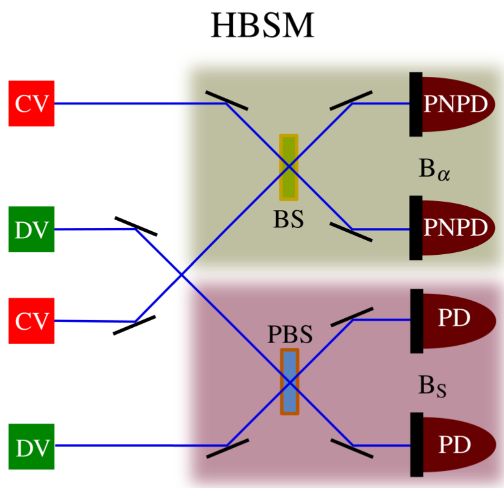

FIG. 3. B_α acts on the CV modes and fails when neither of the two PNPDs click. Its failure rate on the hybrid qubits is $e^{-2\alpha^2}$ [15]. B_S acts on the DV modes and is successful with probability 1/2 only when both the PDs click. A HBSM fails only when both B_α and B_S fail. Thus the failure rate of a HBSM is $e^{-2\alpha^2}/2$.

hybrid BSM (HBSM) and the setup is as shown in Fig. 3. For brevity, we coin this scheme as hybrid-qubit-based topological QC with postselection and n-HBSM EO (PHTQC-n). In principle, we can have n subvariants of the scheme. However, we shall consider only two in this work, namely, PHTQC-2 and PHTQC-3 because those with $n \geqslant 3$ may not offer resource efficiency over the similar DV-qubit-based schemes [41].

In PHTQC-n, implementing $|\mathcal{C}_{\mathcal{L}}\rangle$ commences with the creation of a $4n$-arm star cluster state $|\mathcal{C}_*\rangle_{4n}$, where $n = 1, 2, 3, \ldots$. The state represented by $|\mathcal{C}_*\rangle_{4n}$ has a central qubit and $4n$ number of surrounding arm qubits. The arm qubits are entangled with the central qubit and are represented by the edges, as shown in Fig. 4. Furthermore, the cluster state $|\mathcal{C}_{\mathcal{L}}\rangle$ is formed by entangling the central qubits of multiple $|\mathcal{C}_*\rangle_{4n}$. This EO or creation of edges between the central qubits is achieved by performing multiple HBSMs to which n-arm qubits of each $|\mathcal{C}_*\rangle_{4n}$ are inputs, as shown in Fig. 4. Thus, only the central qubit of $|\mathcal{C}_*\rangle_{4n}$ stays in $|\mathcal{C}_{\mathcal{L}}\rangle$. It is important to note that we perform up to n HBSMs in a sequence until one succeeds or all are exhausted.

A. Hybrid Bell-state measurement

HBSM is a composite of two BSM operations: B_S and B_α acting on DV and CV parts of a hybrid qubit, respectively, as shown in Fig. 3. The failure rate of HBSM drastically approaches to zero with an increasing value of α [15,16]. The measurement B_α comprises a beam splitter (BS) and two photon-number parity detectors (PNPDs), whereas B_s has a polarizing beam splitter (PBS), two photodetectors (PDs). A B_α is successful when one of the two PNPDs clicks and is a failure when both do not click. A successful B_α can have four possible outcomes (combination of PNPD clicks) which corresponds to a projection onto the Bell states, $|\psi^\pm\rangle = |\alpha,\alpha\rangle \pm |-\alpha,-\alpha\rangle$, $|\phi^\pm\rangle = |\alpha,-\alpha\rangle \pm |-\alpha,\alpha\rangle$ (up to normalization). A B_s succeeds only when both PDs click, and all other cases are deemed to be failure. For more details on

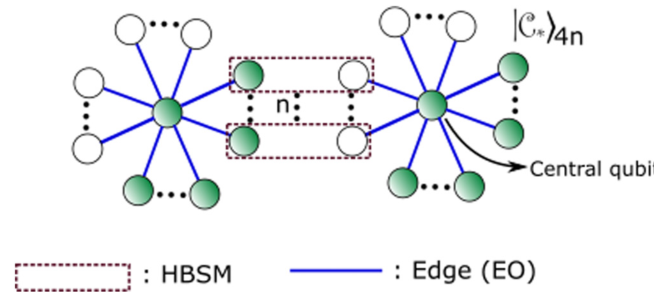

FIG. 4. A $4n$-arm star cluster state $|\mathcal{C}_*\rangle_{4n}$ has a central qubit and $4n$ number of surrounding arm qubits. The arm qubits are entangled with the central qubit via edges. An edge between the two central qubits is created by performing multiple HBSMs to which n arm qubits of each $|\mathcal{C}_*\rangle_{4n}$ are inputs, as shown. In the process, the HBSMs are performed in a sequence until one of them succeeds or all the n-arm qubits are exhausted. This will boost the success rate of the edge creation. Even though the BSMs in linear optics are probabilistic, using multi-HBSM EOs make the edge creation near-deterministic. A multi-HBSM EO fails when all the n constituent HBSMs fail. If p_f is the failure rate of HBSM, the success rate of multi-HBSM EO is $1 - p_f^n$. Thus, a $|\mathcal{C}_{\mathcal{L}}\rangle$ is built by entangling the $|\mathcal{C}_*\rangle_{4n}$ with their four nearest neighbors.

HBSM refer to Refs. [15,16]. Given that the CV and DV parts of hybrid qubits are correlated, HBSM succeeds even when one of B_α and B_s is successful or both of them are successful. A HBSM fails only when both the constituent modules B_α and B_s fail. More precisely, the failure rate of B_α at which no click is registered on the PNPDs is $e^{-2\alpha^2}$ and that of B_s at which only one detector or none clicks is 1/2 [16]. Thus, the failure rate of HBSM turns out to be $e^{-2\alpha^2}/2$. It is important to note that a HBSM failure is heralded so that the knowledge is available for decoding during postselection, multi-HBSM EOs and QEC.

B. Postselection

Star cluster states $|\mathcal{C}_*\rangle_{4n}$ are generated by performing HBSMs on the three-hybrid-qubit cluster states (see Sec. IV for details). Note that HBSMs are not deterministic and there are instances of failure. Importantly, failure of a HBSM on three-hybrid-qubit cluster states leads to $|\mathcal{C}_*\rangle_{4n}$ with missing edges between the central qubit and arm qubits, and also misplaced edges between the arm qubits [refer to Fig. 1(b) of Ref. [16]]. These missing and misplaced edges in turn lower the fault tolerance of $|\mathcal{C}_{\mathcal{L}}\rangle$ [16]. Therefore, discarding such distorted star cluster states becomes crucial for improving the performance parameters. For this we employ postselection, i.e., states are fed to the next stage of star-cluster construction conditioned on all HBSMs being successful. In this way, we can have intact $|\mathcal{C}_*\rangle_{4n}$ (as in Fig. 4) available for forming $|\mathcal{C}_{\mathcal{L}}\rangle$. In optics, postselection over the successful HBSMs can be realized by using *optical delay lines* and *switching circuits* [41].

C. Multi-hybrid Bell-state measurement entanglement operators

As BSMs are not deterministic in linear optics, failures of EOs leave the corresponding edges between the qubits of

$|\mathcal{C}_{\mathcal{L}}\rangle$ missing. This problem of missing edges can be addressed by transforming them to missing qubits of $|\mathcal{C}_{\mathcal{L}}\rangle$ [39]. Then, topological QEC is carried out as detailed in Sec. II. When the missing fraction of the lattice qubits is 0.249 or more, $|\mathcal{C}_{\mathcal{L}}\rangle$ cannot support FTQC [42]. In Ref. [16], HTQC overcomes this problem by using hybrid qubits on which BSM is near-deterministic due to larger value of α. Thus, having only four arms in the star cluster ($|\mathcal{C}_*\rangle_4$) suffices. But, smaller values of α would be appreciable for a better $\eta_{\rm th}$ (see Sec. V). Alternatively, when the BSM is probabilistic, Refs. [39,41,43,44] tackle the problem by having multi-BSM EOs to improve the success rate of edge creation. Similarly, in PHTQC-n we employ n-HBSM EOs so that we can afford smaller values of α and still have edge creation near-deterministically. Suppose that p_f is the failure rate of an individual HBSM in n-HBSM EO. This EO would fail only if all the constituent HBSMs fail. Therefore, the success rate of the n-HBSM EO is $1-p_f^n$, where p_f is $e^{-2\alpha^2}/2$ when there is no photon loss. Under photon loss, p_f is substituted by Eq. (8). The smaller the value of α, the larger n should be to make the n-HBSM EO near-deterministic.

In this n-HBSM EO stage, HBSMs are performed sequentially until one succeeds or all n arm qubits are exhausted, as shown in Fig. 4. With this strategy the incurred resources, in terms of both qubits and BSM trials, grow exponentially as the success rate of BSM falls. Moreover, once a HBSM is successful, all other arm qubits must be removed using Z measurements [43] because an even number of successful HBSMs correspond to removal of the edge. Additionally, one must employ optical delay lines and a switching circuit for sequencing the multiple BSMs. Switching is also known to be a major contributor for photon loss [41]. However, if the success rate of the BSM is high, the complexity of the switching circuit, and hence the photon loss, can be reduced. In this work we study in detail how PHTQC-n performs against photon loss in spite of the apparent former disadvantage.

D. Measurements on hybrid qubits of $|\mathcal{C}_{\mathcal{L}}\rangle$

The measurements on the hybrid qubits of $|\mathcal{C}_{\mathcal{L}}\rangle$ for topological FTQC can be achieved in two ways; either by measuring the DV or CV modes. Measurements on the DV mode are accomplished by detecting the polarization of the photons in their respective basis. For CV modes, X measurements can be achieved by detections on PNPDs, and Z measurements by homodyne detection in the displacement quadrature [22]. Measurements in the $(X \pm Y)/\sqrt{2}$ basis can be achieved by using the displacement operation in photon counting [45] of the CV modes. However, measurements on the DV modes alone are sufficient for carrying out PHTQC-n.

E. In-line and off-line processes

The process of building $|\mathcal{C}_{\mathcal{L}}\rangle$ consists of two stages: offline and inline stages. During the offline stage, two types of three-hybrid-qubit cluster states are generated using $|\Psi_\alpha\rangle$ in Eq. (2) as raw resources [16]. This offline process involves EOs that are probabilistic in nature (see supplemental material of Ref. [16] for details). Failure of an EO would result in a missing edge in these states. To feed intact three-hybrid-qubit cluster states to the next stage we need to postselect on the successful EOs. Once there is a continuous supply of the offline resource states (three-hybrid-qubit cluster states), the inline stage commences by creating copies of $|\mathcal{C}_*\rangle_{4n}$ and entangling them to form lattice qubits and edges. Using $4n-2$ HBSMs on $4n-1$ offline resource states, $|\mathcal{C}_*\rangle_{4n}$ can be generated by postselecting on all successful HBSMs. For example, $|\mathcal{C}_*\rangle_4$ can be generated by using two HBSMs on the off-line resource states, as shown in Fig. 5. Furthermore, $|\mathcal{C}_*\rangle_8$ can be generated using two $|\mathcal{C}_*\rangle_4$ and a three-hybrid qubit cluster state, and two HBSMs as shown in Fig. 6; a total of six HBSMs are required.

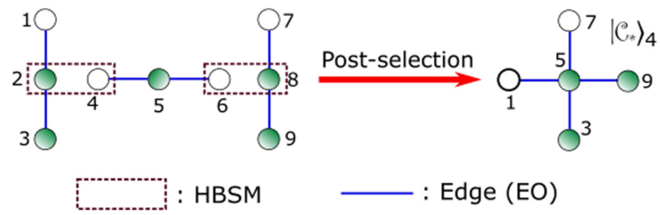

FIG. 5. An unfilled circle represents a qubit on which the Hadamard gate is applied. The three-hybrid-qubit offline resource state with an unfilled circle represents $|\mathcal{C}_3\rangle$ while that with two the $|\mathcal{C}_{3'}\rangle$ [refer to text below Eq. (3)]. Success of both HBSMs create a four-arm star-cluster state $|\mathcal{C}_*\rangle$ and other cases lead to undesired states, as shown in Fig. 1(b) of Ref. [16]. In this work, we postselect on both HBSMs being successful and other cases are discarded.

IV. GENERATION OF STAR CLUSTER STATE

First, we describe in detail how to create $|\mathcal{C}_*\rangle_4$ using offline resource states and HBSMs. This procedure is similar to that in HTQC but involves postselection. Subsequently, we show how to extend the procedure to create $|\mathcal{C}_*\rangle_8$ and, more generally, to create $|\mathcal{C}_*\rangle_{4n}$ with $n>2$.

A $|\mathcal{C}_*\rangle_4$ is created by using two kinds of offline resource states and two HBSMs, as shown in Fig. 5. The two offline resource states have the form

$$\begin{aligned}|\mathcal{C}_3\rangle &= \frac{1}{2}(|\alpha,\alpha,\alpha\rangle|\mathrm{H,H,H}\rangle + |\alpha,\alpha,-\alpha\rangle|\mathrm{H,H,V}\rangle \\ &\quad + |-\alpha,-\alpha,\alpha\rangle|\mathrm{V,V,H}\rangle - |-\alpha,-\alpha,-\alpha\rangle|\mathrm{V,V,V}\rangle),\\ |\mathcal{C}_{3'}\rangle &= \frac{1}{\sqrt{2}}(|\alpha,\alpha,\alpha\rangle|\mathrm{H,H,H}\rangle + |-\alpha,-\alpha,-\alpha\rangle|\mathrm{V,V,V}\rangle).\end{aligned} \tag{3}$$

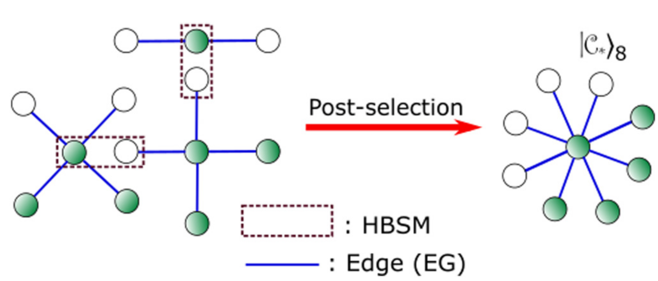

FIG. 6. (a) An eight-arm start cluster state $|\mathcal{C}_*\rangle$ can be created by entangling two four-arm $|\mathcal{C}_*\rangle$ and a three-qubit-cluster state $|\mathcal{C}_{3'}\rangle$ with two HBSMs. Postselection is employed to obtain intact states. Furthermore, copies of eight-arm $|\mathcal{C}_*\rangle$ are entangled to form a $|\mathcal{C}_{\mathcal{L}}\rangle$.

One can verify that $|\mathcal{C}_3\rangle$ is the result of a Hadamard on the first qubit of the three-qubit linear cluster state $\mathrm{CZ}_{2,1}\mathrm{CZ}_{2,3}|+\rangle_1|+\rangle_2|+\rangle_3$. On the other hand, $|\mathcal{C}_{3'}\rangle$ is due to a Hadamard on the first and third qubits of this three-qubit linear cluster state.

It is important to note that the hybrid-qubit-based scheme facilitates the generation of three-qubit cluster states using only linear optics with practical values of α. Although coherent superposition states, $|\alpha\rangle \pm |-\alpha\rangle$ (up to normalization) also support near-deterministic BSM, by using only linear optics it is not possible to generate high-fidelity three-qubit cluster states like $\frac{1}{\sqrt{2}}(|\alpha,\alpha,\alpha\rangle + |\alpha,\alpha,-\alpha\rangle + |-\alpha,-\alpha,\alpha\rangle - |-\alpha,-\alpha,-\alpha\rangle)$ with practical values of α. For example, the scheme in Ref. [22] needs $\alpha \approx 10$ for a fidelity of $\approx$0.9, which is very low for QEC on $|\mathcal{C}_\mathcal{L}\rangle$. For building a $|\mathcal{C}_\mathcal{L}\rangle$ suitable for topological FTQC, one needs initial coherent superposition states of very large α [22]. Moreover, when α is large, dephasing in the presence of photon loss is very strong on the qubits of $|\mathcal{C}_\mathcal{L}\rangle$, resulting in failure of QEC. As such, nonlinear optical schemes like a cavity QED generation scheme [46] are necessary to build a suitable cluster state under those situations. On the other hand, we demonstrate that, by using hybrid qubits of amplitude $\alpha < 1$, it is possible to build a sufficiently good $|\mathcal{C}_\mathcal{L}\rangle$ for topological FTQC.

As shown in Fig. 5, two $|\mathcal{C}_3\rangle$ and a $|\mathcal{C}_{3'}\rangle$ are initialized as $|\mathcal{C}_3\rangle_{1,2,3} \otimes |\mathcal{C}_{3'}\rangle_{4,5,6} \otimes |\mathcal{C}_3\rangle_{7,8,9}$, where $|\mathcal{C}_{3/3'}\rangle_{i,j,k}$ represents the ith, jth, and kth hybrid qubits in the assembly of the cluster states. We perform HBSMs on the hybrid qubits 2, 4 and 6, 8. Out of many possibilities of HBSMs being successful, suppose that they are successful with B_α projecting onto $|\psi^+\rangle$. Then the resulting state of the remaining hybrid qubits 1, 3, 5, 7, and 9 would be

$$\begin{aligned}|\mathcal{C}_*\rangle_4 = {}& |\alpha,\alpha,\alpha,\alpha,\alpha\rangle_{1,3,5,7,9}|\mathrm{H,H,H,H,H}\rangle_{1,3,5,7,9} + |\alpha,\alpha,\alpha,\alpha,-\alpha\rangle_{1,3,5,7,9}|\mathrm{H,H,H,H,V}\rangle_{1,3,5,7,9}\\ &+ |\alpha,-\alpha,\alpha,\alpha,\alpha\rangle_{1,3,5,7,9}|\mathrm{H,V,H,H,H}\rangle_{1,3,5,7,9} + |\alpha,-\alpha,\alpha,\alpha,-\alpha\rangle_{1,3,5,7,9}|\mathrm{H,V,H,H,V}\rangle_{1,3,5,7,9}\\ &+ |-\alpha,\alpha,-\alpha,-\alpha,\alpha\rangle_{1,3,5,7,9}|\mathrm{V,H,V,V,H}\rangle_{1,3,5,7,9} - |-\alpha,\alpha,-\alpha,-\alpha,-\alpha\rangle_{1,3,5,7,9}|\mathrm{V,H,V,V,V}\rangle_{1,3,5,7,9}\\ &- |-\alpha,-\alpha,-\alpha,-\alpha,\alpha\rangle_{1,3,5,7,9}|\mathrm{V,V,V,V,H}\rangle_{1,3,5,7,9} + |-\alpha,-\alpha,-\alpha,-\alpha,-\alpha\rangle_{1,3,5,7,9}|\mathrm{V,V,V,V,V}\rangle_{1,3,5,7,9}. \quad (4)\end{aligned}$$

When the HBSMs are successful with other possibilities of projecting onto different states, the resulting $|\mathcal{C}_*\rangle_4$ would be equivalent to the one in Eq. (4) up to local Pauli rotations. This can be handled by updating the *Pauli frame* without the need for any feed-forward optical operations.

A desired $|\mathcal{C}_*\rangle_4$ with edges connecting the central qubit to all the arm qubits is generated only when both HBSMs are successful. In other cases, that is when one of the HBSMs fails or both, the resulting states are distorted with edges misplaced between surrounding qubits [refer to Fig. 1(b) of Ref. [16]]. To see this, suppose that the HBSM acting on modes 2 and 4 of the initialized state $|\mathcal{C}_3\rangle_{1,2,3} \otimes |\mathcal{C}_{3'}\rangle_{4,5,6} \otimes |\mathcal{C}_3\rangle_{7,8,9}$ fails and the other succeeds. The resulting state is

$$\begin{aligned}(&|\alpha,\alpha\rangle_{1,3}|\mathrm{H,H}\rangle_{1,3} + |\alpha,-\alpha\rangle_{1,3}|\mathrm{H,V}\rangle_{1,3}\\ &+ |-\alpha,\alpha\rangle_{1,3}|\mathrm{V,H}\rangle_{1,3}\\ &+ |-\alpha,-\alpha\rangle_{1,3}|\mathrm{V,V}\rangle_{1,3}) \otimes |\mathcal{C}_3\rangle_{5,7,8}. \quad (5)\end{aligned}$$

We observe that there are no edges (no entanglement) from the central qubit (mode 5) to qubits 1 and 3. Rather, there is a misplaced edge between qubits 1 and 3. We refer to this misplaced edges as diagonal edges due to its geometric appearance [see Fig. 1(b) of Ref. [16]]. This leads to distortion of the lattice geometry and stabilizer structure. Each failure of HBSM results in two missing edges and an undesired diagonal edge in a $|\mathcal{C}_*\rangle_4$. Contrary to Ref. [16], which utilizes distorted star cluster states, here we postselect states on all HBSMs being successful. Due to postselection we are able to choose $|\mathcal{C}_*\rangle_4$ in Eq. (4) which has intact edges and discard the distorted states like that in Eq. (5). Therefore, the resulting $|\mathcal{C}_\mathcal{L}\rangle$ would be free of diagonal edges. Avoiding diagonal edges leads to a lower number of missing lattice edges and in turn to many fewer missing qubits. Therefore, using postselection results in a better $|\mathcal{C}_\mathcal{L}\rangle$ and a better tolerance against dephasing.

Star cluster state with more than four-arm qubits. Increasing the number of arms provides an opportunity to repeat the HBSM operations when the previous ones fail. The bottleneck here is that, as the number of arms goes up, the success rate of HBSMs fall (as α correspondingly decreases) and there is a growing complexity in the switching circuit for postselection. It is also known that switching adds to photon loss, which would be detrimental for η_{th}. For those reasons, we restrict ourselves to utilizing only $|\mathcal{C}_*\rangle_8$ and $|\mathcal{C}_*\rangle_{12}$.

A $|\mathcal{C}_*\rangle_8$ can be created by entangling two $|\mathcal{C}_*\rangle_4$ and a $|\mathcal{C}_{3'}\rangle$ with two HBSMs, as described in Fig. 6, where postselection is carried out over the successful HBSMs. Similar to the case of $|\mathcal{C}\rangle_4$, one can explicitly work out and show that the process in Fig. 6 would result in $|\mathcal{C}_*\rangle_8$. By the same token, one can generate $|\mathcal{C}_*\rangle_{12}$ by entangling $|\mathcal{C}_*\rangle_8$, $|\mathcal{C}_*\rangle_4$, and $|\mathcal{C}_{3'}\rangle$ with two HBSMs.

After building $|\mathcal{C}_\mathcal{L}\rangle$ using $|\mathcal{C}_*\rangle_{4n}$ with postselection, both QEC and gate operations on the topological states of the lattice are executed by measuring the hybrid qubits individually. The measurements, in principle, transfers the state on a layer to the next in a similar manner as in teleportation. In practice, two layers of $|\mathcal{C}_\mathcal{L}\rangle$ suffice at any instant. The third-dimension of $|\mathcal{C}_\mathcal{L}\rangle$ is a happening in time [35].

V. NOISE MODEL

The predominant errors in optical quantum computing models originate from photon loss [1]. In this section, we study the effect of the photon loss on hybrid qubits and in turn on PHTQC-n. The action of the photon-loss channel $\mathcal{E}$ on a hybrid qubits initialized to the state $\rho_0 = |\Psi_\alpha\rangle\langle\Psi_\alpha|$ gives [15]

$$\begin{aligned}\mathcal{E}(\rho_0) = &\frac{(1-\eta)}{2}(|\alpha', \text{H}\rangle\langle\alpha', \text{H}| + |-\alpha', \text{V}\rangle\langle-\alpha', \text{V}| \\ &+ e^{-2\eta\alpha^2}(|\alpha', \text{H}\rangle\langle-\alpha', \text{V}| + |-\alpha', \text{V}\rangle\langle\alpha', \text{H}|)) \\ &+ \frac{\eta}{2}[(|\alpha'\rangle\langle\alpha'| + |-\alpha'\rangle\langle-\alpha'|) \otimes |0\rangle\langle 0|], \\ = &(1-\eta)\left(\frac{1+e^{-2\eta\alpha^2}}{2}|\Psi^+_{\alpha'}\rangle\langle\Psi^+_{\alpha'}| \right. \\ &\left. + \frac{1-e^{-2\eta\alpha^2}}{2}|\Psi^-_{\alpha'}\rangle\langle\Psi^-_{\alpha'}|\right) \\ &+ \frac{\eta}{2}(|\Phi^+_{\alpha'}\rangle\langle\Phi^+_{\alpha'}| + |\Phi^-_{\alpha'}\rangle\langle\Phi^-_{\alpha'}|), \end{aligned} \tag{6}$$

where $|\Psi^\pm_{\alpha'}\rangle = (|\alpha', \text{H}\rangle \pm |-\alpha', \text{V}\rangle)/\sqrt{2}$, $|\Phi^\pm_{\alpha'}\rangle = |0\rangle \otimes (|\alpha'\rangle \pm |-\alpha'\rangle)/\sqrt{2}$, and $\alpha' = \sqrt{1-\eta}\alpha$ with η being the photon-loss rate that arises from imperfect sources and detectors, absorptive optical components, and storage. The effect of photon loss on hybrid-qubits is to introduce phase-flip errors Z and diminishes the amplitude α to α', which consequently lowers the success rate of HBSMs. Its also forces the hybrid qubit state to leak out of the computational basis $\{|0\rangle_\text{L}, |1\rangle_\text{L}\}$.

From Eq. (6) one can deduce that the dephasing rate is

$$p_z = (1-\eta)\frac{1-e^{-2\eta\alpha^2}}{2} + \frac{\eta}{2} = \frac{1}{2}[1-(1-\eta)e^{-2\eta\alpha^2}], \tag{7}$$

which increases with the value of α for a given η. Thus, for a fixed value of η, we face a trade-off between the desirable success rate of HBSM and the detrimental effects of dephasing with increasing value of α. Owing to photon loss, the failure rate of a HBSM reads

$$p_f = \tfrac{1}{2}(1-\eta)e^{-2\alpha'^2} + \eta e^{-2\alpha'^2} = \tfrac{1}{2}(1+\eta)e^{-2\alpha'^2}. \tag{8}$$

In the above equation, the first term originates from the attenuation of the CV part, while the second from both CV attenuation and DV loss. We point out that, like DV optical schemes [44], photon loss does not necessarily imply lattice-qubit loss in PHTQC-n. The probability $\langle 0,0|\mathcal{E}(\rho_0)|0,0\rangle = \eta e^{-\alpha'^2}$ that photon loss leading to lattice-qubit loss for $\eta \sim 10^{-3}$ is much smaller than the HBSM failure rate p_f and can be neglected.

VI. SIMULATION OF QUANTUM ERROR CORRECTION

To simulate QEC on the $|\mathcal{C}_\mathcal{L}\rangle$ of hybrid-qubits with missing edges and dephasing noise, we use the software package AUTOTUNE [47]. It offers a wide range of options for noise models and their customization to suit our scheme. Most importantly, it allows for the simulation of QCE when the qubits are missing. We obtain results by exploiting this feature *via* mapping missing edges to missing qubits [48].

AUTOTUNE uses the circuit model (where qubits are initialized in the $|+\rangle$ state and CZ operations are applied to create entanglement between the appropriate qubits) to simulate the error propagation during the formation of $|\mathcal{C}_\mathcal{L}\rangle$. Here, we detail how noise in PHTQC-n (which employs techniques different from the circuit model for building $|\mathcal{C}_\mathcal{L}\rangle$) can be simulated using AUTOTUNE. As explained in Sec. III, only the central hybrid qubit of $|\mathcal{C}_*\rangle_{4n}$ remains in the lattice and the arm qubits are utilized by the HBSMs. All the hybrid qubits of $|\mathcal{C}_*\rangle_{4n}$ suffer from dephasing of rate p_Z in Eq. (7) due to photon loss. The action of HBSMs transfer noise on the arm qubits to the central qubits [16]. Thus, the central qubits accumulate additional noise due to the HBSMs. The role of a HBSM in creating edges between the central qubits of $|\mathcal{C}_*\rangle_{4n}$ is equivalent to that of a CZ in the circuit model for building $|\mathcal{C}_\mathcal{L}\rangle$. So, the action of HBSMs under noise in PHTQC can be simulated by noisy CZs in AUTOTUNE. Once a noisy $|\mathcal{C}_\mathcal{L}\rangle$ is simulated, the QEC proceeds the same way for both pictures. AUTOTUNE also allows for the simulation of noise introduced during the initialization of qubits that mimics a noisy $|\mathcal{C}_*\rangle_{4n}$ and subsequent error propagation through the action of HBSMs. Other operations in AUTOTUNE that are not relevant to us are set to be noiseless.

More specifically, noise from a HBSMs is simulated as noise introduced by a CZ described by the Kraus operators $\{\sqrt{(1-2p_Z)}I \otimes I,\ \sqrt{p_Z}Z \otimes I,\ \sqrt{p_Z}I \otimes Z\}$ [16]. In PHTQC-n, HBSMs act up to n times to create an edge between two central qubits. The rate of dephasing added by n HBSMs on the central qubits is $1-(1-p_Z)^n$. In the limit $p_Z \ll 1$, this amounts to np_Z. Accordingly, the noise corresponding to n HBSMs would have the following Kraus operators: $\{\sqrt{(1-2np_Z)}I \otimes I,\ \sqrt{np_Z}Z \otimes I,\ \sqrt{np_Z}I \otimes Z\}$. However, it is not necessary to perform all n HBSMs available in PHTQC-n. When one of the available n succeeds, we stop performing HBSMs. The second HBSM is performed with probability $1-p_f$ when the first one fails, and so on. Therefore, the average number of HBSMs needed to create an edge is

$$\begin{aligned} n_\text{avg} &= \sum_{m=0}^{n-1}(1-p_f)p_f^m(m+1) \\ &= 1-(n+1)p_f^n + \frac{p_f}{1-p_f}(1-p_f)^n \\ &\approx 1+p_f \\ &\approx \frac{1}{1-p_f} \text{ for } p_f \ll 1. \end{aligned} \tag{9}$$

Thus, in PHTQC-n, a noisy entangling operation is described by the set of Kraus operators: $\{\sqrt{(1-2n_\text{avg}p_Z)}I \otimes I,\ \sqrt{n_\text{avg}p_Z}Z \otimes I,\ \sqrt{n_\text{avg}p_Z}I \otimes Z\}$. As $n_\text{avg} < n$ for small p_f, this strategy of stopping the HBSM process after one succeeds will help in reducing the dephasing noise due to HBSMs. This description also accounts for dephasing in the switching process. AUTOTUNE also allows us to simulate instances when no gate actions happen, but qubits suffer loss and dephasing. We assume that the postselection takes place in this instance. This allows us to account for photon loss and dephasing during the switching process in the simulation.

Furthermore, the QEC simulation on a faulty $|\mathcal{C}_\mathcal{L}\rangle$ begins by making X-basis measurements on the noisy hybrid qubits. We again introduce dephasing of rate p_Z on the hybrid qubits waiting to undergo measurement. The X-measurement outcomes used for syndrome extraction during QEC could be erroneous. This error rate is also set to p_Z. Due to photon loss, the hybrid qubits may leak out of the logical basis which makes measurements on such DV modes impossible. This

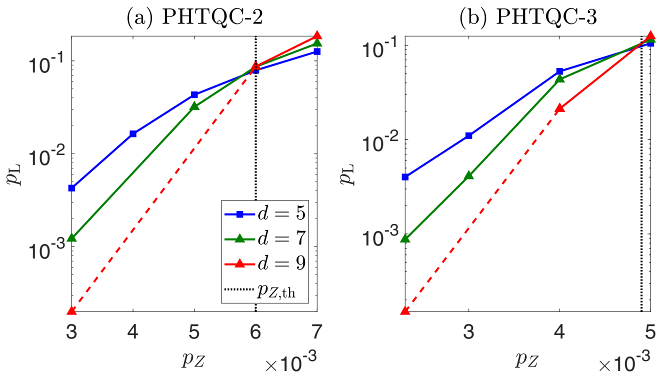

FIG. 7. Logical error rate p_L is plotted against the dephasing rate p_Z for PHTQC-2 and PHTQC-3 of code distances $d = 5, 7, 9$. The intersecting point of these curves corresponds to the threshold dephasing rate $p_{Z,\mathrm{th}}$. The plots correspond to the qubit loss rate $p_{\mathrm{loss}} = 0.03$.

leakage error too is assigned the same rate of p_Z. As $p_Z > \eta$, the assignment will only overestimates the leakage error of rate η.

VII. RESULTS FOR PHOTON LOSS THRESHOLD

The *logical error* rate p_L is determined against the value of p_Z for $|\mathcal{C}_{\mathcal{L}}\rangle$ of code distances d using AUTOTUNE. This calculation is repeated for various values of lattice-qubit loss rate p_{loss}, which correspond to different values of α. The intersection point of the curves corresponding to various d is the threshold dephasing rate $p_{Z,\mathrm{th}}$ as marked in Fig. 7. The photon-loss threshold η_{th} is determined using Eq. (7) by replacing p_Z with $p_{Z,\mathrm{th}}$.

From Fig. 3(b) of Ref. [16], we estimate that PHTQC-n would also perform best around $p_{\mathrm{loss}} = 0.03$ because both schemes use the same error model. Thus, we simulate the QEC for both PHTQC-2 and PHTQC-3 with $p_{\mathrm{loss}} = 0.03$. To determine the values of α required for PHTQC-n, we map p_{loss} to p_f as detailed in the following.

Each qubit in $|\mathcal{C}\rangle_{\mathcal{L}}$ is associated with four edges created by n-HBSM. When all HBSMs fail the edge between the lattice qubits will be missing. In this scenario, either of the qubits is removed with equal probability thereby mapping a missing edge to a missing qubit [48]. In PHTQC-n, the probability of having a missing edge is p_f^n. A qubit is removed when more than one of the associated edges is missing, giving us

$$p_{\mathrm{loss}} = 1 - \left(1 - \frac{1}{2}p_f^n\right)^4. \tag{10}$$

After inserting the values of p_{loss} and n into Eq. (10), we find that PHTQC-2 and PHTQC-3 require α of 0.84 and 0.6, respectively. From the simulation result for PHTQC-2, as shown in Fig. 7(a), we have $p_{Z,\mathrm{th}} = 0.006$, which translates to $\eta_{\mathrm{th}} = 5 \times 10^{-3}$ with the aid of Eq. (7). Similarly, from Fig. 7(b) we have $p_{Z,\mathrm{th}} = 0.0049$, which results in $\eta_{\mathrm{th}} = 5.7 \times 10^{-3}$ for PHTQC-3. These results imply that the PHTQC-2 and PHTQC-3 schemes provide improved values of η_{th} over HTQC. Compared with other known optical QC schemes [15,21,44,49–52], we find that PHTQC-3 provides the highest η_{th} (when the computational error rate is nonzero).

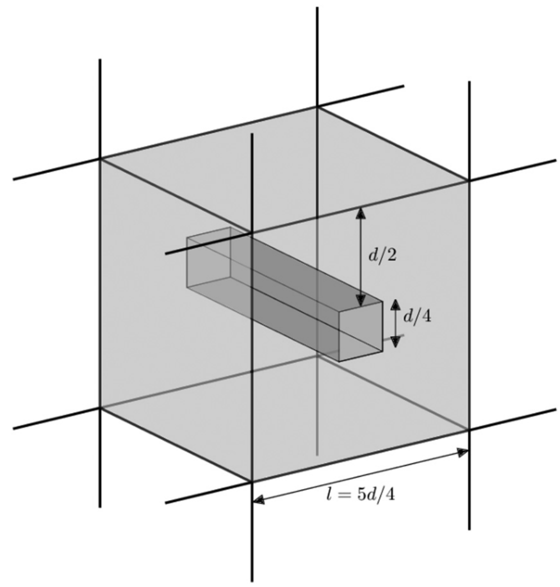

FIG. 8. To achieve fault tolerance for gate operations, both the circumference of a defect and distance between two defects should be d. So, the defects are placed in the cubic lattice of side $l = 5d/4$ as shown such that distance between the defects is d. Thus on average, a cubic lattice of volume $(5d/4)^3$ is required per fault tolerant gate operation.

VIII. RESULTS ON RESOURCE OVERHEAD

To estimate the resource overhead per fault-tolerant topological gate operation, we count the average number of hybrid qubits N required to build a cubic fraction of the $|\mathcal{C}\rangle_{\mathcal{L}}$ of sufficiently large side l determined by the target p_L. As depicted in Fig. 8, l is determined such that the cubic fraction can accommodate a defect of circumference d so that there are no error chains encircling it. Also, the defect is separated by a distance d [33] from those in neighboring cubic fractions to avoid a chain of errors connecting them. For this, the side of the cubic fraction must be at least $l = 5d/4$. By extrapolating the suppression of p_L with d, we determine the value of d required to achieve the target $p_L \approx 10^{-15}$ using the following expression [33] (see also Fig. 7):

$$p_L = \frac{b}{\left(\frac{a}{b}\right)^{\frac{d-d_b}{2}}}, \tag{11}$$

where a and b are the values of p_L corresponding to the second highest and the highest code distances d_a and d_b, respectively, chosen for our simulations. We determine a and b below half the threshold value, that is $p_{Z,\mathrm{th}}/2$. Once d is determined, N can be estimated as detailed in the subsequent section. We emphasize that N also depends upon the value of the η at which FTQC schemes operate, that is closer to threshold they operate, more resources are consumed.

TABLE I. The table lists various fault-tolerant optical QC schemes, the associated QEC codes, type of optical resource used, the optimal photon loss threshold $\eta_{\rm th}$ they provide and incurred resource overhead N. The resource overhead N to attain the logical error rate $p_{\rm L} \sim 10^{-6}(10^{-15})$ is calculated for operational values of the photon loss rate η and computational error rate. It should be noted that $\eta_{\rm th}$ claimed by OCQC, PLOQC, EDQC, and TPQC (in *italic*) are valid only for zero computational errors, which is unrealistic since photon losses would cause computational errors. It is clear that PHTQC-3 offer highest η and computational error rate by an order of magnitude compared with other known optical QC schemes along with the best resource efficiency. Note that, in PHTQC-n with an $n > \mathbf{3}$ value of failure rate of HBSM, p_f is comparable to that in DV scheme [41] and the usage of hybrid qubits offers no advantage in significantly reducing N. We hence only provide results up to $n = 3$.

Scheme	QEC Code	$\eta_{\rm th}$	η, computational error rate	Resource	N for $p_{\rm L} = 10^{-6}$	N for $p_{\rm L} = 10^{-15}$
OCQC	7-qubit Steane code	4×10^{-3}	4×10^{-4}, 4×10^{-5}	Bell pair	2.6×10^{19}	7.1×10^{24}
PLOQC	7-qubit Steane code	2×10^{-3}	4×10^{-4}, 4×10^{-5}	Bell pair	6.8×10^{14}	3.5×10^{19}
EDQC	Error detecting codes	1.57×10^{-3}	1×10^{-4}, 1×10^{-5}	Bell pair	$O(10^{13})$	$O(10^{16})$
CSQC	7-qubit Steane code	2.3×10^{-4}	8×10^{-5}, 1.97×10^{-5}	CSS qubits	2.1×10^{11}	6.9×10^{15}
MQQC	7-qubit Steane code	1.7×10^{-3}	$O(10^{-4})$, $O(10^{-4})$	Bell pair	2.7×10^{14}	1.4×10^{19}
HQQC	7-qubit Steane code	4.6×10^{-4}	$O(10^{-4})$, $O(10^{-4})$	Hybrid qubits	8.2×10^{9}	2.3×10^{12}
TPQC	Topological	5.3×10^{-4}	0, 1×10^{-3} (5.3×10^{-4}, 0)	Entangled photons	$>2\times10^{9}$	$>4.2\times10^{10}$
HTQC	Topological	3.3×10^{-3}	1.5×10^{-3}, 3×10^{-3}	Hybrid qubits	8.5×10^{5}	1.7×10^{7}
PHTQC-2	Topological	5×10^{-3}	2.4×10^{-3}, 3×10^{-3}	Hybrid qubits	1.1×10^{6}	1.8×10^{7}
PHTQC-3	Topological	$\mathbf{5.7}\times10^{-3}$	2.6×10^{-3}, 2.3×10^{-3}	Hybrid qubits	2.9×10^{7}	4.9×10^{8}

Resource overhead for PHTQC-*n*

Let us recall that two $|\mathcal{C}_3\rangle$, a $|\mathcal{C}_{3'}\rangle$ and two HBSMs are needed to create $|\mathcal{C}_*\rangle_4$. The success rate of both HBSMs is $(1-\frac{1}{2}e^{-2\alpha'^2})^2$. On average, $8/[(1-e^{-2\alpha'^2})^2]$ hybrid qubits are needed to create a $|\mathcal{C}_3\rangle$ or $|\mathcal{C}_{3'}\rangle$. Taking postselection into account, the average number of hybrid qubits in building $|\mathcal{C}_*\rangle_4$ would be $24/[(1-e^{-2\alpha'^2})^2(1-\frac{1}{2}e^{-2\alpha'^2})^2]$. In general, a $|\mathcal{C}_*\rangle_{4n}$ can be created by entangling a $|\mathcal{C}_*\rangle_{4n-4}$, a $|\mathcal{C}_*\rangle_4$ and a $|\mathcal{C}_{3'}\rangle$ using two HBSMs. A $|\mathcal{C}_*\rangle_{4n-4}$ in turn requires $4n-6$ HBSMs, while $|\mathcal{C}_*\rangle_4$ needs two HBSMs. Therefore, a total of $4n-2$ HBSMs are used in creating $|\mathcal{C}_*\rangle_{4n}$, which is formed from n $|\mathcal{C}_*\rangle_4$ and $n-1$ $|\mathcal{C}_{3'}\rangle$. On average, one needs

$$\left[\frac{24n}{(1-e^{-2\alpha'^2})^2}+\frac{8(n-1)}{(1-e^{-2\alpha'^2})^2}\right]\frac{1}{\left(1-\frac{1}{2}e^{-2\alpha'^2}\right)^{4n-2}}$$

hybrid qubits to synthesize $|\mathcal{C}_*\rangle_{4n}$.

As mentioned in Sec. III, each $|\mathcal{C}_*\rangle_{4n}$ appears as a single qubit in the final lattice $|\mathcal{C}_{\mathcal{L}}\rangle$. This means the number of $|\mathcal{C}_*\rangle_{4n}$ needed to build a lattice of side l is $6l^3$. Finally, the average number of hybrid qubits needed for building $|\mathcal{C}_{\mathcal{L}}\rangle$ of side $l = 5d/4$ in PHTQC-n is

$$N_n = \left[\frac{32n-8}{(1-e^{-2\alpha'^2})^2}\right]\frac{125d^3}{64\left(1-\frac{1}{2}e^{-2\alpha'^2}\right)^{4n-2}}, \qquad (12)$$

which is more than that for HTQC.

For PHTQC-2, the value of amplitude of hybrid qubits is set to $\alpha = 0.84$ so that $p_{\rm loss} = 0.03$ and then $p_{\rm L}$ is determined against dephasing. From the simulation result in Fig. 7(a) we have $p_{\rm L}$ corresponding to $|\mathcal{C}_{\mathcal{L}}\rangle$ of distance $d_a = 7$ to be $a \approx 1.2\times10^{-3}$ and that corresponding to $d_b = 9$ is $b \approx 2\times10^{-4}$. Using these values in Eq. (11), we estimate that $|\mathcal{C}_{\mathcal{L}}\rangle$ of $d \approx 15\,(39)$ is needed to achieve $p_{\rm L} \sim 10^{-6}\,(10^{-15})$. Using these values of α and d in the Eq. (12), we estimate that $N_2 \approx 1.1\times10^6\,(1.8\times10^7)$ hybrid qubits are incurred in PHTQC-2.

Similarly, for PHTQC-3, we set $\alpha = 0.6$ such that $p_{\rm loss} = 0.03$ and then $p_{\rm L}$ is determined against dephasing. From Fig. 7(b) we have $a \approx 8.5\times10^{-3}$ when $d_a = 7$ and $b \approx 1.7\times10^{-4}$ when $d_b = 9$. As in the previous case, using these values we estimate that $|\mathcal{C}_{\mathcal{L}}\rangle$ of $d \approx 16\,(41)$ is needed to achieve $p_{\rm L} \approx 10^{-6}\,(10^{-15})$. Thus PHTQC-3 incurs $N_3 \approx 2.9\times10^7\,(4.9\times10^8)$ hybrid qubits.

IX. COMPARISON

We briefly present the known linear optical FTQC schemes based on DV, CV and hybrid platforms and compare their performance parameters (tabulated in Table I) with those of PHTQC-n.

Reference [49] is one of the earliest works that determines the threshold region of η and computational error rate and performs resource estimation for linear optical QC. The scheme uses optical *cluster states* [26] for FTQC (which we abbreviate as OCQC), built using entangled polarization photon pairs. This scheme uses CSS QEC codes [2] coupled with telecorrection, where teleportation is used for error-syndrome extraction for fault tolerance. OCQC uses concatenation of QEC codes to attain low values of $p_{\rm L}$. For example, 6 (4) levels of error correction were employed to attain $p_{\rm L} \sim 10^{-15}\,(10^{-6})$. Unfortunately, resource overhead N demanded by OCQC (see Table I) is too high for practical purposes and subsequent studies aimed to reduce it.

Later, Ref. [50] used *error-detecting quantum state transfer* (EDQC) for optical FTQC. The underlying codes were capable of detecting errors in a way similar to the scheme in Ref. [53], where QEC is shown to be possible by concatenating different error-detecting codes. EDQC offers a smaller $\eta_{\rm th}$, but the value of N could be reduced by many orders of magnitude compared with OCQC (refer to Table I). Another scheme, namely, the parity state linear optical QC (PLOQC) scheme [51] that encodes multiple photons into a logical qubit in *parity state*, provides a smaller $\eta_{\rm th}$, but an improved resource efficiency compared with OCQC. This scheme, similar to OCQC, uses CSS QEC codes and telecorrection. There also exists the multiphoton qubit QC (MQQC) scheme [52] that uses telecorrection based on CSS QEC code. See Table I for the parameters of performance of MQQC. Similar to OCQC, schemes EDQC, PLOQC, and MQQC need few levels of concatenation of QEC codes to attain target p_L (refer to supplemental material of Ref. [16] for details). Using DV optical platform a topological photonic QC (TPQC) scheme was proposed [44]. In Ref. [44], photonic topological QC (TPQC) scheme operating on a DV optical platform was proposed. Here, FTQC is performed on $|\mathcal{C}_{\mathcal{L}}\rangle$ built from a stream of entangled polarization photons. The value of N for TPQC is calculated either for $\eta = 0$ or zero computational error rate (only those cases are considered in the Ref. [44]). When both the parameters are nonzero, N would in principle be much larger.

The coherent-state quantum computation (CSQC) [19–21] uses the following set of coherent states $\{|\alpha\rangle, |-\alpha\rangle\}$ as the logical basis for CV qubits. CSQC also executes telecorrection for tolerance against photon loss and computational errors [21]. In this CV scheme, superpositions of superposition states, $|\alpha\rangle \pm |-\alpha\rangle$ (up to normalization) [54,55], are considered as resources. This reduces N by many orders of magnitude compared with OCQC, but at the cost of a lower $\eta_{\rm th}$. As seen from Table I, the $\eta_{\rm th}$ is smaller by an order of magnitude than OCQC.

A hybrid-qubit-based QC (HQQC) [15] scheme uses optical hybrid states instead of coherent superposition states. HQQC offers a better value of $\eta_{\rm th}$ and resource scaling than CSQC. If different kinds of hybrid qubits [56] are employed for telecorrection, one would speculate a better resilience against photon loss in HQQC. In linear optical FTQC, the recent HTQC [16] offers the best $\eta_{\rm th}$ and resource efficiency known to date. However, PHTQC-2 and PHTQC-3 lead to even better $\eta_{\rm th}$ than HTQC at the cost of incurring slightly more resources. Nevertheless, the new schemes remain resource efficient, in marked contrast with all other linear optical schemes for FTQC.

We stress caution by noting that, in OCQC, PLOQC, EDQC, and TPQC, the two noise parameters η and the computational error rate are independent. However, these parameters are interdependent in HTQC, PHTQC, CSQC, HQQC, and MBQC. Moreover, in the former schemes, the computational error is depolarizing in nature whereas in the latter schemes, it is a result of dephasing caused by photon loss. It is important to note $\eta_{\rm th}$ claimed by OCQC, PLOQC, EDQC, and TPQC are valid only for zero computational errors, which is unrealistic since photon losses typically cause computational errors.

X. DISCUSSION AND CONCLUSION

In pushing hybrid qubit quantum computing to the limit, we establish postselection schemes for the creation of star cluster states and utilize multiple hybrid Bell-state measurements per edge creation to build a Raussendorf lattice for fault-tolerant quantum computation. Compared to a recently published hybrid qubit scheme [16], we show that our current hybrid scheme with postselection can achieve an even higher photon-loss threshold. In particular, we achieve the threshold values of 5×10^{-3} and 5.7×10^{-3} with two respective subvariants of the scheme, namely, PHTQC-2 and PHTQC-3 introduced in this work. They represent an approximately 50% improvement compared with the previous scheme without postselection (3.3×10^{-3}) [16].

This enhancement comes from the desirable fact that the hybrid-qubit scheme with postselection can have a high success rate of entangling operations without the need to use hybrid qubits of large coherent amplitudes. Consequently, the current scheme benefits from weaker dephasing effects arising from photon loss. We also show that a larger photon loss threshold comes at a nominal increase in resource overhead of about one order of magnitude in comparison with that for the hybrid qubit scheme without postselection. In terms of hardware design, this additionally requires switching circuits to support postselection and multiple hybrid Bell-state measurements. Therefore, the ballistic character of the previous hybrid qubit scheme is sacrificed in exchange for higher photon-loss tolerance.

From these findings, we now confirm that all hybrid-qubit schemes permit significantly higher operational photon loss and computational error rates, by an order of magnitude compared with other optical schemes [15,21,44,49–52]. Although the optical-cluster scheme [49] provides a slightly larger photon-loss threshold compared with the previous ballistic hybrid-qubit scheme [16], we have shown that our current scheme can provide an even larger threshold values. We also demonstrate an overall superiority in resource efficiency of our current scheme. If the failure rate of hybrid Bell-state measurements is large, postselection of higher intensity is required and would render its performance comparable to discrete variable schemes. Eventually, using hybrid qubits offers no resource advantage over the discrete variable scheme in Ref. [41].

In hindsight, since using smaller coherent amplitudes in postselection hybrid schemes boosts photon-loss thresholds, it naturally supports the logic that a Raussendorf lattice built with only discrete-variable qubits could offer an even higher photon loss threshold, albeit at higher resource costs.

Proposals to generate optical hybrid states, without cross-Kerr nonlinearity, using only linear optical elements and photon detectors, were made in Refs. [57–60]. Sophisticated manipulations of time-bin and wave-like degrees of freedom have also opened interesting routes to generating such entangled states [61–67]. These achievements pave the way to practical hybrid qubit quantum computing.

ACKNOWLEDGMENTS

We thank Austin G. Fowler for useful discussions and suggestions. This work was supported by National Research Foundation of Korea (NRF) grants funded by the Korea government (Grants No. 2019M3E4A1080074, No. 2020R1A2C1008609, and No. 2020K2A9A1A06102946) via the Institute of Applied Physics at Seoul National University. Y.S.T. was supported by a NRF grant funded by the Korea government (Grant No. NRF-2019R1A6A1A10073437). S.W.L. acknowledges support from the National Research Foundation of Korea (2020M3E4A1079939) and the KIST institutional program (2E31021).

[1] T. C. Ralph and G. J. Pryde, Optical Quantum Computation, Prog. Optics **54**, 209 (2010).

[2] M. A. Nielsen and I. L. Chuang, *Quantum Computation and Quantum Information* (Cambridge University Press, 2010).

[3] *Quantum Error Correction*, edited by D. A. Lidar and T. A. Brun (Cambridge University Press, Cambridge, 2013).

[4] S. Zhou, M. Zhang, J. Preskill, and L. Jiang, Achieving the Heisenberg limit in quantum metrology using quantum error correction, Nat. Commun. **9**, 78, (2018).

[5] K. C. Tan, S. Omkar, and H. Jeong, Quantum-error-correction-assisted quantum metrology without entanglement, Phys. Rev. A **100**, 022312 (2019).

[6] S. Muralidharan, J. Kim, N. Lütkenhaus, M. D. Lukin, and L. Jiang, Ultrafast And Fault-Tolerant Quantum Communication Across Long Distances, Phys. Rev. Lett. **112**, 250501 (2014).

[7] F. Ewert and P. van Loock, Ultrafast fault-tolerant long-distance quantum communication with static linear optics, Phys. Rev. A **95**, 012327 (2017).

[8] S.-W. Lee, T. C. Ralph, and H. Jeong, Fundamental building block for all-optical scalable quantum networks, Phys. Rev. A **100**, 052303 (2019).

[9] S. Omkar, R. Srikanth, and S. Banerjee, Characterization of quantum dynamics using quantum error correction, Phys. Rev. A **91**, 012324 (2015).

[10] S. Omkar, R. Srikanth, and S. Banerjee, Quantum code for quantum error characterization, Phys. Rev. A **91**, 052309 (2015).

[11] S. Omkar, R. Srikanth, S. Banerjee, and A. Shaji, The two-qubit amplitude damping channel: Characterization using quantum stabilizer codes, Ann. Phys. (NY) **373**, 145 (2016).

[12] A. Shabani and D. A. Lidar, Maps for general open quantum systems and a theory of linear quantum error correction, Phys. Rev. A **80**, 012309 (2009).

[13] S. Omkar, R. Srikanth, and S. Banerjee, The operator-sum-difference representation of a quantum noise channel, Quantum Inf. Process. **14**, 2255 (2015).

[14] M. A. Nielsen and C. M. Dawson, Fault-tolerant quantum computation with cluster states, Phys. Rev. A **71**, 042323 (2005).

[15] S.-W. Lee and H. Jeong, Near-deterministic quantum teleportation and resource-efficient quantum computation using linear optics and hybrid qubits, Phys. Rev. A **87**, 022326 (2013).

[16] S. Omkar, Y. S. Teo, and H. Jeong, Resource-Efficient Topological Fault-Tolerant Quantum Computation With Hybrid Entanglement Of Light, Phys. Rev. Lett. **125**, 060501 (2020).

[17] R. Knill, E.and Laflamme and G. J. Milburn, A scheme for efficient quantum computation with linear optics, Nature (London) **409**, 46 (2001).

[18] H. Jeong, M. S. Kim, and J. Lee, Quantum-information processing for a coherent superposition state via a mixedentangled coherent channel, Phys. Rev. A **64**, 052308 (2001).

[19] H. Jeong and M. S. Kim, Efficient quantum computation using coherent states, Phys. Rev. A **65**, 042305 (2002).

[20] T. C. Ralph, A. Gilchrist, G. J. Milburn, W. J. Munro, and S. Glancy, Quantum computation with optical coherent states, Phys. Rev. A **68**, 042319 (2003).

[21] A. P. Lund, T. C. Ralph, and H. L. Haselgrove, Fault-Tolerant Linear Optical Quantum Computing With Small-Amplitude Coherent States, Phys. Rev. Lett. **100**, 030503 (2008).

[22] C. R. Myers and T. C. Ralph, Coherent state topological cluster state production, New J. Phys. **13**, 115015 (2011).

[23] A. M. Steane, Error Correcting Codes In Quantum Theory, Phys. Rev. Lett. **77**, 793 (1996).

[24] A. R. Calderbank and P. W. Shor, Good quantum error-correcting codes exist, Phys. Rev. A **54**, 1098 (1996).

[25] A. Steane, Multiple-particle interference and quantum error correction, Proc. R. Soc. London, Ser. A **452**, 2551 (1996).

[26] R. Raussendorf and H. J. Briegel, A One-Way Quantum Computer, Phys. Rev. Lett. **86**, 5188 (2001).

[27] J. Joo and D. L. Feder, Error-correcting one-way quantum computation with global entangling gates, Phys. Rev. A **80**, 032312 (2009).

[28] K. Fujii and K. Yamamoto, Cluster-based architecture for fault-tolerant quantum computation, Phys. Rev. A **81**, 042324 (2010).

[29] D. S. Wang, A. G. Fowler, and L. C. L. Hollenberg, Surface code quantum computing with error rates over 1%, Phys. Rev. A **83**, 020302(R) (2011).

[30] J. L. O'Brien, Optical quantum computing, Science **318**, 1567 (2007).

[31] X.-C. Yao, T.-X. Wang, H.-Z. Chen, W.-B. Gao, A. G. Fowler, R. Raussendorf, Z.-B. Chen, N.-L. Liu, C.-Y. Lu, Y.-J. Deng, Y.-A. Chen, and J.-W. Pan, Experimental demonstration of topological error correction, Nature (London) **482**, 489 (2012).

[32] A. G. Fowler and K. Goyal, Topological cluster state quantum computing, Quantum Inf. Comput. **9**, 721 (2009).

[33] A. C. Whiteside and A. G. Fowler, Upper bound for loss in practical topological-cluster-state quantum computing, Phys. Rev. A **90**, 052316 (2014).

[34] H. J. Briegel, D. E. Browne, W. Dür, R. Raussendorf, and M. Van den Nest, Measurement-based quantum computation, Nat. Phys. **5**, 19 (2009).

[35] R. Raussendorf, J. Harrington, and K. Goyal, A fault-tolerant one-way quantum computer, Ann. Phys. (NY) **321**, 2242 (2006).

[36] R. Raussendorf, J. Harrington, and K. Goyal, Topological fault-tolerance in cluster state quantum computation, New J. Phys. **9**, 199 (2007).

[37] R. Raussendorf and J. Harrington, Fault-Tolerant Quantum Computation With High Threshold in Two Dimensions, Phys. Rev. Lett. **98**, 190504 (2007).

[38] S. D. Barrett and T. M. Stace, Fault Tolerant Quantum Computation With Very High Threshold for Loss Errors, Phys. Rev. Lett. **105**, 200502 (2010).

[39] Y. Li, S. D. Barrett, T. M. Stace, and S. C. Benjamin, Fault Tolerant Quantum Computation With Nondeterministic Gates, Phys. Rev. Lett. **105**, 250502 (2010).

[40] J. Edmonds, Maximum matching and a polyhedron with 0, 1-vertices, J. Res. Natl. Bur. Stand., Sect. B **Sect. B 69B**, 125 (1965).

[41] Y. Li, P. C. Humphreys, G. J. Mendoza, and S. C. Benjamin, Resource Costs For Fault-Tolerant Linear Optical Quantum Computing, Phys. Rev. X **5**, 041007 (2015).

[42] C. D. Lorenz and R. M. Ziff, Precise determination of the bond percolation thresholds and finite-size scaling corrections for the SC, FCC, and BCC lattices, Phys. Rev. E **57**, 230 (1998).

[43] K. Fujii and Y. Tokunaga, Fault-Tolerant Topological One-Way Quantum Computation With Probabilistic Two-Qubit Gates, Phys. Rev. Lett. **105**, 250503 (2010).

[44] D. A. Herrera-Martí, A. G. Fowler, D. Jennings, and T. Rudolph, Photonic implementation for the topological cluster-state quantum computer, Phys. Rev. A **82**, 032332 (2010).

[45] S. Izumi, M. Takeoka, K. Wakui, M. Fujiwara, K. Ema, and M. Sasaki, Projective measurement onto arbitrary superposition of weak coherent state bases, Sci. Rep. **8**, 2999 (2018).

[46] P. Munhoz, F. Semião, A. Vidiella-Barranco, and J. Roversi, Cluster-type entangled coherent states, Phys. Lett. A **372**, 3580 (2008).

[47] A. G. Fowler, A. C. Whiteside, A. L. McInnes, and A. Rabbani, Topological Code Autotune, Phys. Rev. X **2**, 041003 (2012).

[48] J. M. Auger, H. Anwar, M. Gimeno-Segovia, T. M. Stace, and D. E. Browne, Fault-tolerant quantum computation with nondeterministic entangling gates, Phys. Rev. A **97**, 030301(R) (2018).

[49] C. M. Dawson, H. L. Haselgrove, and M. A. Nielsen, Noise thresholds for optical cluster-state quantum computation, Phys. Rev. A **73**, 052306 (2006).

[50] J. Cho, Fault-tolerant linear optics quantum computation by error-detecting quantum state transfer, Phys. Rev. A **76**, 042311 (2007).

[51] A. J. F. Hayes, H. L. Haselgrove, A. Gilchrist, and T. C. Ralph, Fault tolerance in parity-state linear optical quantum computing, Phys. Rev. A **82**, 022323 (2010).

[52] S.-W. Lee, K. Park, T. C. Ralph, and H. Jeong, Nearly Deterministic Bell Measurement For Multiphoton Qubits And Its Application To Quantum Information Processing, Phys. Rev. Lett. **114**, 113603 (2015).

[53] E. Knill, Quantum computing with realistically noisy devices, Nature (London) **434**, 39 (2005).

[54] B. Yurke and D. Stoler, Generating Quantum Mechanical Superpositions Of Macroscopically Distinguishable States Via Amplitude Dispersion, Phys. Rev. Lett. **57**, 13 (1986).

[55] A. Ourjoumtsev, H. Jeong, R. Tualle-Brouri, and P. Grangier, Generation of optical 'Schrödinger cats' from photon number states, Nature (London) **448**, 784 (2007).

[56] H. Kim, S.-W. Lee, and H. Jeong, Two different types of optical hybrid qubits for teleportation in a lossy environment, Quantum Inf. Process. **15**, 4729 (2016).

[57] H. Kwon and H. Jeong, Generation of hybrid entanglement between a single-photon polarization qubit and a coherent state, Phys. Rev. A **91**, 012340 (2015).

[58] S. Li, H. Yan, Y. He, and H. Wang, Experimentally feasible generation protocol for polarized hybrid entanglement, Phys. Rev. A **98**, 022334 (2018).

[59] K. Huang, H. L. Jeannic, O. Morin, T. Darras, G. Guccione, A. Cavaillès, and J. Laurat, Engineering optical hybrid entanglement between discrete- and continuous-variable states, New J. Phys. **21**, 083033 (2019).

[60] S. A. Podoshvedov and N. B. An, Designs of interactions between discrete- and continuous-variable states for generation of hybrid entanglement, Quantum Inf. Process. **18**, 68 (2019).

[61] H. Jeong, A. Zavatta, M. Kang, S.-W. Lee, L. S. Costanzo, S. Grandi, T. C. Ralph, and M. Bellini, Generation of hybrid entanglement of light, Nat. Photonics **8**, 564 (2014).

[62] O. Morin, K. Huang, J. Liu, H. Le Jeannic, C. Fabre, and J. Laurat, Remote creation of hybrid entanglement between particle-like and wave-like optical qubits, Nat. Photonics **8**, 570 (2014).

[63] A. E. Ulanov, D. Sychev, A. A. Pushkina, I. A. Fedorov, and A. I. Lvovsky, Quantum Teleportation Between Discrete and Continuous Encodings of an Optical Qubit, Phys. Rev. Lett. **118**, 160501 (2017).

[64] D. V. Sychev, A. E. Ulanov, E. S. Tiunov, A. A. Pushkina, A. Kuzhamuratov, V. Novikov, and A. I. Lvovsky, Entanglement and teleportation between polarization and wave-like encodings of an optical qubit, Nat. Commun. **9**, 3672 (2018).

[65] A. Cavaillès, H. Le Jeannic, J. Raskop, G. Guccione, D. Markham, E. Diamanti, M. D. Shaw, V. B. Verma, S. W. Nam, and J. Laurat, Demonstration Of Einstein-Podolsky-Rosen Steering Using Hybrid Continuous- and Discrete-Variable Entanglement of Light, Phys. Rev. Lett. **121**, 170403 (2018).

[66] G. Guccione, T. Darras, H. Le Jeannic, V. B. Verma, S. W. Nam, A. Cavaillès, and J. Laurat, Connecting heterogeneous quantum networks by hybrid entanglement swapping, Sci. Adv. **6**, eaba4508 (2020).

[67] E. Gouzien, F. Brunel, S. Tanzilli, and V. D'Auria, Scheme for the generation of hybrid entanglement between time-bin and wavelike encodings, Phys. Rev. A **102**, 012603 (2020).